Power Electronic Systems
Laboratory

IEEE Transactions on Power Electronics, Vol. 34, No. 1, pp. 438-451, January 2019

Performance Evaluation of Series-Compensated IPT Systems for Transcutaneous Energy Transfer

O. Knecht,
J. W. Kolar

Eidgenössische Technische Hochschule Zürich
Swiss Federal Institute of Technology Zurich

Performance Evaluation of Series-Compensated IPT Systems for Transcutaneous Energy Transfer

Oliver Knecht, *Student Member, IEEE* and Johann W. Kolar, *Fellow, IEEE*

***Abstract*— Today's implantable mechanical circulatory support devices, such as Left Ventricular Assist Devices (LVADs) still rely on a percutaneous driveline, which is a frequent cause of severe infections and which reduces the quality of life for the patients. Inductive Power Transfer (IPT) is therefore a promising technology to replace the driveline and hence, reducing the likelihood of an infection. The focus of this paper is on the series-series compensated IPT system and provides an in-depth comparison of two operating modes, i.e. the operation at resonance and the operation above resonance, and highlights the advantages and disadvantages with respect to the requirements set by the application at hand. In addition, the paper presents the design and the realization of a fully functional TET implant hardware prototype, which includes the IPT front-end, the control circuit, the backup battery and its charging converter, as well as the communication electronics in a boxed volume of only 10.3 cl. The experimental verification shows that overall DC-DC efficiencies of up to 90 % can be achieved for both operating modes when transmitting 25-30 W from the external battery to the implant backup battery, each having a nominal voltage of 14.8 V, using TET coils with 70 mm diameter and 10 mm coil separation distance.**

***Index Terms*—Transcutaneous energy transfer, inductive power transfer**

I. Introduction

Concurrently to the ageing society in the industrial nations, the number of people suffering from severe heart failures has increased. At the end stage, a heart transplantation is often the only effective treatment. However, the number of suitable donor hearts is limited. The recently published Eurotransplant Annual Report 2016 [1] shows, that since 2003, the number of patients awaiting a donor heart has almost doubled, whereas the number of heart transplants has stagnated since then. This trend promoted the further development of implantable Mechanical Circulatory Support (MCS) systems, such as Left Ventricular Assist Devices (LVAD). **Fig. 1(a)** shows the illustration of a typical MCS system with an implanted LVAD that allows to support the weakened heart and to maintain the regular blood circulation in the human body. A major problem with today's LVAD therapy is the risk of severe infections, which are likely to occur at the exit site of the percutaneous driveline, which is used to power the blood pump [2]. The evaluation of the INTERMACS registry data in the period from 2006 to 2010 by Goldstein et al. [3] has shown, that after the first year, still 19 % of the 2006 patients who received the HeartMate II LVAD have suffered from a driveline infection, with a mean time 6.6 months until the percutaneous site infection occurs.

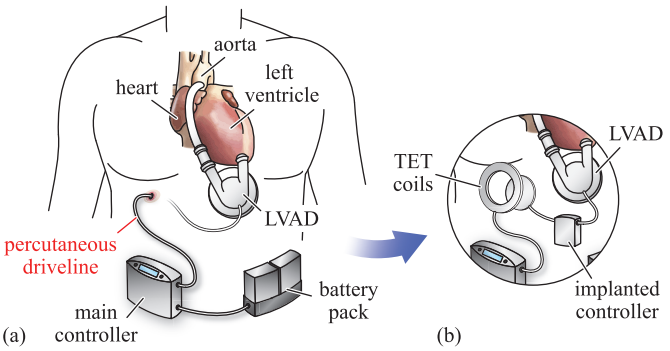

Figure 1: (a) Mechanical Circulatory Support (MCS) system as it is used today, including the LVAD and the percutaneous driveline, which is required to power the implanted blood pump. (b) Fully implantable MCS system, incorporating a Transcutaneous Energy Transfer (TET) system, i.e a wireless energy transmission system for powering the LVAD.

Consequently, Inductive Power Transfer (IPT) technology has emerged as a promising solution for powering the LVAD without the need for a galvanic contact [4], as it is illustrated in **Fig. 1(b)**, and allows to implement a Transcutaneous Energy Transfer (TET) system as a next step towards a fully implantable MCS system. The basic structure of a typical TET system is shown in **Fig. 2**. The key part is the IPT system including an inverter, a rectifier and the IPT resonant circuit, including the energy transmission coils. The TET system further contains the power management circuit, i.e. additional DC-DC converter stages, which are needed to control the IPT system. On the secondary side, a backup battery is included that allows for a temporary completely untethered operation of the implant. Today's state-of-the-art LVADs have a continuous power consumption of 4-12W [5], [6], but for bi-ventricular support or in case of a Total Artificial Heart (TAH), the power consumption can be significantly higher. Therefore, the TET system described in this work is designed for a total power transfer capability of up to 30 W, in order to allow for the operation of the LVAD and the simultaneous charging of the implanted backup battery.

In addition to the power management system, the TET system includes one or more uni- or bidirectional wireless communication interfaces, which allow for a feedback control of the IPT system and can be employed for transmitting physiological sensor data, which can be utilized for controlling

O. Knecht was with the Power Electronic Systems Laboratory, Swiss Federal Institute of Technology (ETH) Zurich, 8092 Zurich, Switzerland. He is now with Onefive GmbH (part of NKT Photonics S/A), 8105 Regensdorf, Switzerland (e-mail: oknecht@swissonline.ch).

J. W. Kolar is with the Power Electronic Systems Laboratory, Swiss Federal Institute of Technology (ETH) Zurich, 8092 Zurich, Switzerland (e-mail: kolar@lem.ee.ethz.ch).

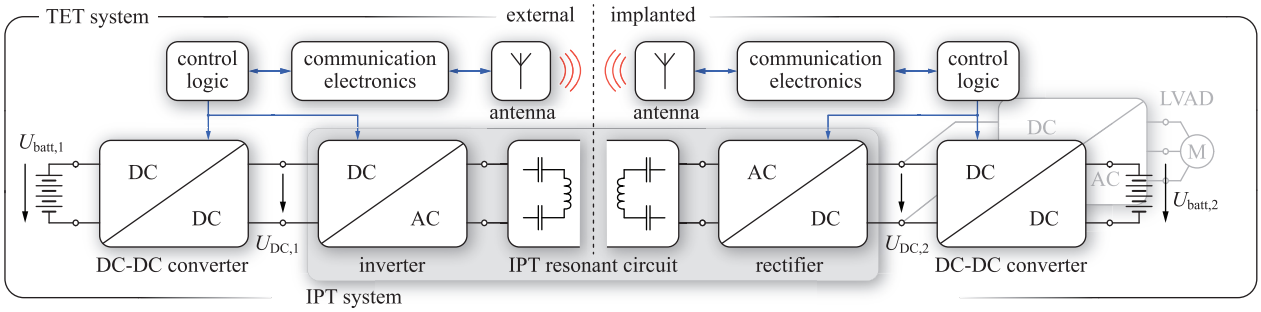

Figure 2: Basic power management concept of the Transcutaneous Energy Transfer (TET) system.

the LVAD. The power electronic inverter, which is used to drive the LVAD is either connected in parallel to the internal backup battery, or directly to the output of the IPT system, depending on the selected system topology.

The requirements for the TET implant are particularly challenging and the design targets and optimization objectives are briefly summarized in the following:

- **Energy efficiency** is the major performance characteristic of the TET system. Specifically for the targeted power transfer levels at hand, high power losses within the implant or the energy transfer coils can cause discomfort to the patient, or in case of excessive heating, may even cause permanent tissue damage.
- **Coil misalignment** has a big impact on the IPT system performance, since the magnetic coupling of the energy transfer coils is directly related to the geometric arrangement of the two coils. For the application at hand, it is expected that the nominal distance between the perfectly axially aligned coils is 10 mm, but the system must be designed to allow for coil separation distances of up to 20-30 mm.
- **System volume** is a critical parameter for all implantable medical devices. Considering the number and the volume of the electronic components (cf. **Fig. 2**), the TET system implant volume will be considerably larger than today's pacemakers or Implantable Cardioverter-Defibrillators (ICDs).
- **System reliability** is particularly important, since in this case, the implant has to continuously process a considerable amount of electrical power and a failure within the implanted electronic system is immediately life-threatening and provokes a surgical intervention.
- **System safety** is closely related to the system reliability. Due to the high power transfer capability, several safety risks are associated with the TET system operation, such as high operating voltages within the IPT system, excessive heating of the tissue or the exposure of the human body to strong electromagnetic fields.

In the past, several prototype IPT and/or TET systems for MCS system have been designed and were tested at different stages of development, but up-to-date no TET system is on the marked and approved for clinical use. **Tab. I** gives an overview of the IPT system implementations found in the literature [7]–[16] and summarizes the main characteristics, such as the IPT coil diameter, coil separation distance, output power, operating frequency and the achieved DC-DC efficiency at the specified operating point. It is important to note that a direct comparison of the different IPT system designs is difficult and in most cases would be unfair. Hence, **Tab. I** serves more to give the reader an impression of the range of the key design and performance parameters achieved in the past.

year of publication	prim. coil Ø (mm)	sec. coil Ø (mm)	core material	coil distance (mm)†	operating frequency (kHz)	output power (W)	DC-DC efficiency (%)
1993 [7,8]	90	66	none	15	437	18	76
2000 [9]	90	60	none	14	430	36	61
2006 [10]	90	72	ferrite	20	160	27	86
2009 [11]	64	64	ferrite	20	285	24	89
2009 [12]	92	53	ferrite	15	163	20	85
2010 [13]	50	50	none	20	200	15	84
2012 [14]	65	50	none	20	386 ††	15	79
2014 [15]	95	55	none	20	790	16	82
2015 [16]	88	66	none	15	600	29	84

† coil separation distance at perfect axial alignment.
†† presumed from the specifications given in [14].

Table I: Specifications and performance overview of previously developed TET systems for the use with MCS systems [7]–[16].

It was shown in [17] that the series-series compensated IPT circuit topology outperforms the secondary side parallel compensated systems for the considered maximum output power of 30 W. Therefore, the focus of this paper is on the performance evaluation and the comparison of two operating modes of the series-series compensated IPT system. The operating modes are comprehensively compared regarding several performance metrics, such as the energy transfer efficiency, the secondary side coil power loss and the secondary side coil voltage stress. Each operating mode is investigated in detail in **Section II**, and the control concept for the IPT system and the proposed overall TET system topology is explained for the both operating modes. In **Section III**, the hardware realization of the TET implant prototype is presented and **Section IV** shows the performance measurements of the TET system. Concluding remarks are given in **Section V**.

II. Series-series compensated IPT system

The design and the operation of the series-series compensated IPT circuit topology, which is shown in **Fig. 3(a)**, is described in detail in [17], [18] and is intuitively explained in the following for the two considered operating modes.

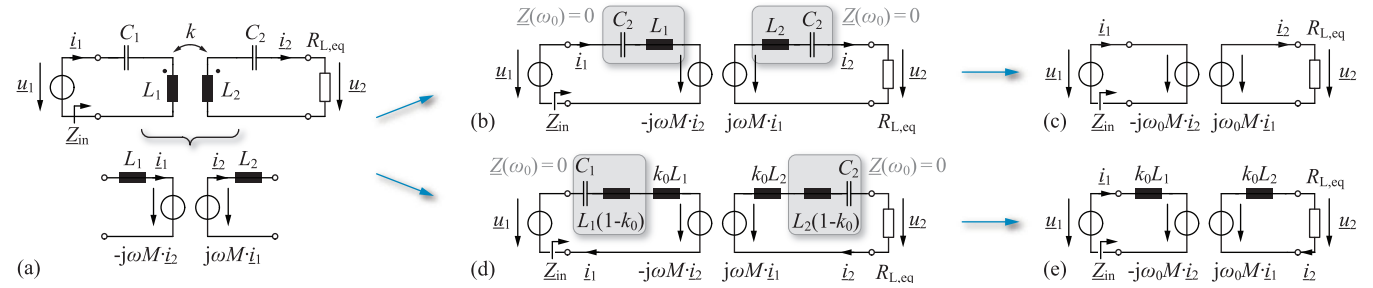

Figure 3: (a) Series-series compensated IPT resonant circuit topology and transformer equivalent circuit. (b)-(c) Equivalent circuit for the series-series compensated topology operated at the resonant frequency (denoted as SSR operation) and the same circuit designed for operation above the resonant frequency (d)-(e), (denoted as SSU operation).

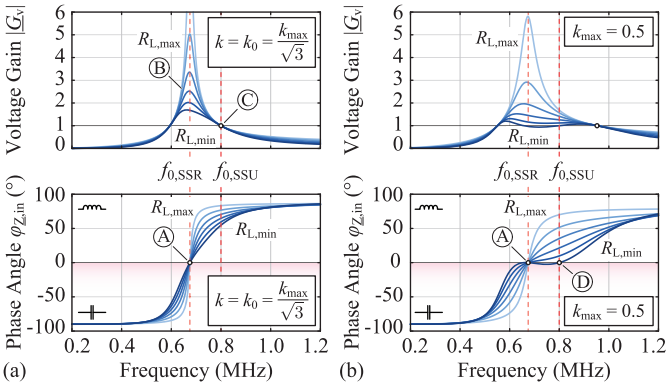

(c)

Parameter	Value	Parameter	Value
L_1, L_2	18.4 µH	$f_{0,SSU}$	800 kHz
C_1, C_2	3.0 nF	k_{max}	0.50
$U_{DC,2}$	37.4 V	k_0	0.29

Figure 4: (a)-(b) Typical voltage transfer characteristics and phase angle of the input impedance of the series-series compensated IPT circuit topology, calculated for different coil coupling factors and the IPT system specifications provided in (c), given an output power range of 5-30 W and a constant output voltage of $U_{DC,2} = 37.4\,\mathrm{V}$.

A. Operation at Resonance

For the operation at the resonance frequency of the IPT resonant circuit, the impedance of the self-inductance of the primary and secondary IPT coils are fully compensated by the resonant capacitors at the desired operating frequency $\omega_0 = 2\pi f_0$, as indicated in **Fig. 3(b)**. Accordingly, the compensation capacitors are selected according to

$$C_i = \frac{1}{\omega_0^2 L_i}\,, \quad i \in [1,2]\,. \tag{1}$$

In the following, this particular mode of operation is referred to as SSR operation. The equivalent circuit at the operating frequency is depicted in **Fig. 3(c)**, which reveals the current source behaviour of the IPT resonant circuit, i.e. at a fixed coil coupling, the secondary side coil current is independent of the load resistance $R_{L,eq}$ and can be controlled directly by adjusting the input voltage $\underline{u}_1$ according to

$$\underline{i}_2 = \mathrm{j}\frac{\underline{u}_1}{\omega_0 M}\,, \tag{2}$$

where $M = k\sqrt{L_1 L_2}$ denotes the mutual inductance of the magnetically coupled IPT coils. The input impedance $\underline{Z}_{in}$ at the operating frequency depends on the load resistance and on the coil coupling factor and is purely resistive, i.e. the input voltage $\underline{u}_1$ and the input current $\underline{i}_1$ are in phase, independent of the operating conditions. Typical voltage transfer characteristics of the series-series compensated IPT circuit topology are shown in **Fig. 4(a)** and **(b)**, calculated for different coil coupling factors and the IPT system specifications provided in **Fig. 4(c)**, given a variable load resistance and a constant IPT system output voltage. The specific voltage transfer characteristics of the SSR operation are clearly visible in **Fig. 4(a)**, such as the purely resistive input impedance at the operating frequency $f_{0,SSR}$, indicated with (A), and the large voltage gain variation (B), which is due to the current source behaviour of the system.

Assuming a lossless operation of the resonant circuit as well as purely sinusoidal primary and secondary side coil currents with the peak values $\hat{I}_1$ and $\hat{I}_2$, the simplified equivalent circuit in **Fig. 3(c)** can be used to calculate the power that is delivered to the resistive load, as shown in [18]

$$P_2 = \frac{1}{2}\underbrace{\omega_0 M \hat{I}_1}_{\hat{U}_{2,(1)}}\hat{I}_2 = \frac{1}{2}\frac{\hat{U}_{1,(1)}\hat{U}_{2,(1)}}{\omega_0 M}\,, \tag{3}$$

where $\hat{U}_{1,(1)}$ and $\hat{U}_{2,(1)}$ denote the magnitude of the fundamental frequency component of the resonant circuit input and output voltage, which can be calculated approximately with $\hat{U}_{i,(1)} = \frac{4}{\pi}U_{DC,i}$, $i \in [1,2]$, if a full-bridge rectifier and inverter stage with perfectly rectangular input and output voltage waveforms are assumed. Consequently, the equation for the output power (3) can be rearranged to

$$P_2 = \frac{8}{\pi^2}\frac{U_{DC,1}U_{DC,2}}{\omega_0 M}\,. \tag{4}$$

According to (4), the primary and/or the secondary side DC-link voltages $U_{DC,1}$ and $U_{DC,2}$ can be used to control the transmitted power [18]. As mentioned above, due to the current source behaviour of the SSR system, the secondary side DC-link voltage $U_{DC,2}$ can be impressed and/or adjusted by the subsequent converter stage [18], and hence allows to control the equivalent load resistance $R_{L,eq}$ of the IPT system.

The total reactive power, that is provided by the resonant capacitors, is given by

$$q_{tot} = q_{C1} + q_{C2} = \underbrace{\frac{\hat{U}_{2,(1)}^2}{2R_{L,eq}}}_{P_2}\left(\frac{\gamma}{k^2} + \frac{1}{\gamma}\right)\,, \tag{5}$$

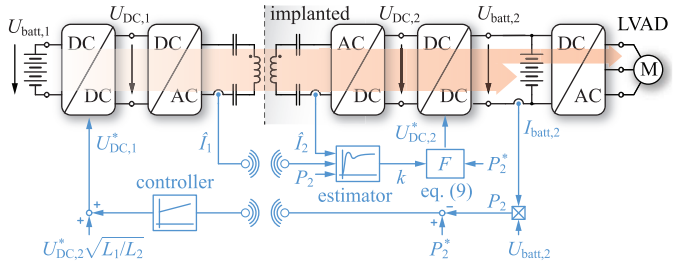

Figure 5: TET system topology using the *efficiency optimal control* for the series-series compensated IPT system operated at resonance (SSR) [18].

where the factor γ is referred to as *load factor* and is defined in [19] with

$$\gamma = \frac{R_{\mathrm{L,eq}}}{\omega_0 L_2} \,. \tag{6}$$

The power transfer efficiency of the IPT system is maximized, if the total reactive power in (5), and hence, the primary and secondary side coil RMS currents, are minimized [20], which is achieved for the optimal load factor given by

$$\gamma_{\mathrm{opt,SSR}} = k \,. \tag{7}$$

In order to achieve an efficiency optimal operation, the load resistance that is presented to the IPT resonant circuit must be adjusted depending on the output power level and the coil coupling factor. This principle of operation is referred to as *efficiency optimal control* and is described in detail in [18]. A brief summary will be given in the following.

Assuming sinusoidal primary and secondary side coil currents and employing a full-wave rectifier at the output of the IPT resonant circuit, a very simple equivalent load model [21], i.e. an equivalent load resistance

$$R_{\mathrm{L,eq}} = \frac{8}{\pi^2}\frac{U^2_{\mathrm{DC},2}}{P_2} \tag{8}$$

can be used to model the load together with the full-wave rectifier.

Combining (6),(7) and (8), the optimum IPT system output DC-link voltage setpoint is calculated according to

$$U^*_{\mathrm{DC,2,SSR}} = \sqrt{\frac{\pi^2}{8} P_2^* k \omega_0 L_2} \,, \tag{9}$$

which is required to provide the load matching for any output power level and coil coupling factor [18]. The input DC-link voltage setpoint $U^*_{\mathrm{DC},1}$ is then calculated with [18]

$$U^*_{\mathrm{DC},1} = \sqrt{\frac{L_1}{L_2}} U^*_{\mathrm{DC},2} \,. \tag{10}$$

The implementation of the *efficiency optimal control* according to [18] is illustrated in **Fig. 5**. Additional filtering stages which are required to protect the battery from large voltage and current ripples are not explicitly shown in the figure. A key requirement for the controller implementation is the estimation of the coil coupling factor k, which is needed to evaluate equation (9). The coupling factor can be deduced from equation (3), using the measurements of the output power and the primary and secondary side coil current amplitudes. Accordingly, the optimal IPT system output voltage $U^*_{\mathrm{DC,2,SSR}}$, calculated with equation (9), is set by the secondary side DC-DC converter, in order to set the optimal load resistance for the IPT circuit. The output power setpoint P_2^* is then maintained by adjusting the primary side DC-link voltage $U_{\mathrm{DC},1}$. As stated in [18], the dynamic performance of the SSR system can be improved by including a feed-forward of the primary side DC-link voltage $U^*_{\mathrm{DC},1}$ according to (10).

An interruption of the communication between the primary and secondary side, or a fault condition on the secondary side with a rapid change of the load condition can result in a high voltage at the output of the SSR system, which is due to the large voltage gain of the resonant circuit, and hence, raises questions about the operational safety of the SSR IPT system. In addition, since the input and output voltage vary over a wide range above and also below the primary and secondary side battery voltage range of 12-16.8 V, a buck-boost type DC-DC converter is needed on either side of the IPT resonant converter, as illustrated in **Fig. 5**. In this case, the input voltage of the motor inverter is clamped to the battery voltage and during the battery charging process, both the charging power and the power to drive the LVAD must be supplied by the secondary side DC-DC converter. Consequently, the inductor of the DC-DC converter must be designed for the maximum power rating and hence, a relatively large inductor volume is needed in order to reduce the power loss in the implant.

B. Operation above Resonance

A special case of the series-series compensated IPT circuit topology is the operation above resonance at the operating frequency $f_{0,\mathrm{SSU}}$, which allows for an operation with load independent voltage gain, as reported in [11], [22]–[24], and which is indicated in **Fig. 4(a)** with (C). In order to operate the system at this specific operating point, the compensation capacitors are designed according to

$$C_i = \frac{1}{\omega_0^2 L_i (1-k_0)} \,, \quad i \in [1,2] \,, \tag{11}$$

where the factor k_0 denotes a design parameter that will become more clear in the following. In this case, only a part of the impedance of the primary and secondary side coil self-inductances is compensated at the operating frequency (cf. **Fig. 3(d)**). The basic operating characteristics can be derived from the equivalent circuit shown in **Fig. 3(e)** and the relationship between the input and output voltage is given by

$$\underline{u}_1 = \mathrm{j}\omega_0 \left(k_0 L_1 - \frac{k^2}{k_0} L_1 \right) \cdot \underline{i}_1 + \frac{k}{k_0}\sqrt{\frac{L_1}{L_2}} \cdot \underline{u}_2 \,. \tag{12}$$

The first term in (12) is cancelled if $k = k_0$. In this case, the voltage gain of the resonant circuit becomes

$$|\underline{G}_{\mathrm{v}}| = \left| \frac{\underline{u}_2}{\underline{u}_1} \right|_{k=k_0} = \sqrt{\frac{L_2}{L_1}} \,, \tag{13}$$

and is synonymous with the *operation for load independent voltage gain*. Furthermore, unity gain is achieved if the primary and the secondary side coils have equal self-inductances, and is referred to as SSU operation. Note that in the following, the operation of the series-series compensated IPT system

operated above the resonant frequency around the frequency for load independent voltage gain is always referred to as SSU IPT system operation, regardless of the actual gain of the resonant circuit.

Further note, that with a fixed operating frequency $f_{0,\mathrm{SSU}}$, the load independent voltage gain can be achieved only for $k = k_0$, as shown in **Fig. 4(a)**. If the coil coupling factor k increases, the point of load independent voltage gain will move towards higher frequencies, as shown in **Fig. 4(b)**.

As described in [25], for equal and large coil quality factors, i.e. $Q_1 = Q_2 > 100$, the optimal load factor $\gamma_{\mathrm{opt,SSU}}$ is given by

$$\gamma_{\mathrm{opt,SSU}} = \frac{R_{\mathrm{L,eq,opt}}}{\omega_0 L_2} \approx \sqrt{k^2 + k_0^2}\,. \tag{14}$$

Combining (8) and (14) yields the optimal secondary side inductance, which is given by

$$L_{2,\mathrm{opt}} = \frac{8}{\pi^2} \cdot \frac{U_{\mathrm{DC},2}^2}{\sqrt{2}\omega_0 k_0 P_{2,\mathrm{max}}}\,, \tag{15}$$

at maximum output power $P_{2,\mathrm{max}}$ and at the coupling $k = k_0$.

Using the simplified equivalent circuit in **Fig. 3(e)**, the phase angle of the input impedance $\varphi_{\underline{Z},\mathrm{in}}$ can be derived at the operating frequency ω_0, and is given by [17]

$$\varphi_{\underline{Z},\mathrm{in}} = \arctan\left(\frac{k_0\left(R_{\mathrm{L,eq}}^2 + \left(k_0^2 - k^2\right)\omega_0^2 L_2^2\right)}{k^2 \omega_0 L_2 R_{\mathrm{L,eq}}}\right)\,, \tag{16}$$

which is independent of the primary side coil inductance L_1. At a coil coupling factor of $k = k_0$, the equation for the phase angle of the input impedance is reduced to

$$\varphi_{\underline{Z},\mathrm{in}}\Big|_{k=k_0} = \arctan\left(\frac{R_{\mathrm{L,eq}}}{k_0 \omega_0 L_2}\right)\,, \tag{17}$$

and with the load matched to the secondary side coil inductance according to (15), the phase angle of the input impedance is given by

$$\varphi_{\underline{Z},\mathrm{in}}\Big|_{k=k_0,\,\gamma=\gamma_{\mathrm{opt,SSU}}} = \arctan\left(\sqrt{2}\right) = 54.7^\circ\,. \tag{18}$$

As a consequence, an operation with load independent voltage gain and maximum energy transfer efficiency cannot be achieved at the same time [23], since in this case, the phase angle of the input impedance $\varphi_{\underline{Z},\mathrm{in}}$ given in (16) is only zero if

$$R_{\mathrm{L,eq}} = \omega_0 L_2 \sqrt{k^2 - k_0^2}\,, \tag{19}$$

and is in contradiction with equation (14), unless $k_0 = 0$, which is again equal to the SSR operation.

As shown in **Fig. 4(a)** and **(b)**, the phase angle of the input impedance at the operating frequency $f_{0,\mathrm{SSU}}$ is increasing with decreasing coil coupling factor and with increasing load resistance. Hence, in order to ensure that the phase angle of the input impedance is still positive at maximum output power and at the maximum achievable coupling factor k_{max}, i.e. at the minimum coil separation distance, the design parameter k_0 must be chosen according to [17]

$$k_0 \geq \frac{k_{\mathrm{max}}}{\sqrt{3}}\,. \tag{20}$$

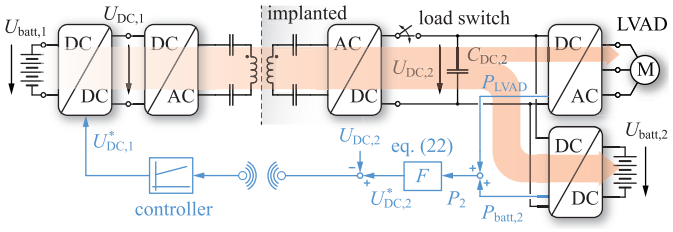

Figure 6: Control structure of the TET system using the series-series compensated IPT system operation above resonance (SSU).

As a result, at maximum output power and maximum coil coupling, the phase angle of the input impedance is exactly zero at the operating frequency, as indicated in **Fig. 4(b)**, denoted with (D). And at $k = k_0 = k_{\mathrm{max}}/\sqrt{3}$, the operation for load independent voltage gain and load matching is achieved. Consequently, the voltage gain variation is kept low for a wide load range and coupling factor variation, and a high energy transfer efficiency can be achieved at the maximum coil coupling factor. However, an operation at exactly zero phase angle of the input impedance is not practical, since it would result in hard-switching operation of the inverter stage. Hence, in order to design the IPT system for a desired input phase angle $\varphi_{\underline{Z},\mathrm{in,d}}$, which is large enough to ensure Zero Voltage Switching (ZVS) operation at maximum output power and maximum coil coupling, the factor k_0 is determined with [17]

$$k_0 = \frac{k_{\mathrm{max}}}{\sqrt{3}} \sqrt{\tan\left(\varphi_{\underline{Z},\mathrm{in,d}}\right)\sqrt{2} + 1}\,. \tag{21}$$

A main drawback of the SSU operation is the increasing reactive power demand at the input of the resonant circuit, which is increasing with decreasing coil coupling factor. Therefore, similar to the *efficiency optimal control*, it is proposed to allow for a variation of the secondary side DC-link voltage according to the output power demand. But in contrast to the SSR IPT system operation, the SSU operation advantageously shows a much lower voltage gain variation with respect to changes of the load conditions and coupling factor, and an estimation of the coil coupling factor is not required for the control of the IPT system. The secondary side DC-link voltage is varied according to the power demand of the load using [25]

$$U^*_{\mathrm{DC,2,SSU}} = \frac{2^{3/4}}{4}\pi \sqrt{P_2 k_0 \omega_0 L_2}\,. \tag{22}$$

As a result, the equivalent load resistance of the SSU compensated resonant circuit is kept at a constant value of

$$R^*_{\mathrm{L,eq,s}} = \sqrt{2} k_0 \omega_0 L_2\,, \tag{23}$$

and this type of operation is therefore referred to as *constant load impedance control*.

The proposed structure and the control scheme of the SSU IPT system is shown in **Fig. 6**. The power consumption of the LVAD and the battery charging converter (i.e. in charging mode), is measured continuously and the set-point for the required IPT system output voltage $U^*_{\mathrm{DC,2,SSU}}$ is calculated using equation (22). On the primary side of the system, a DC-DC converter is then used to control the secondary side DC-link voltage accordingly.

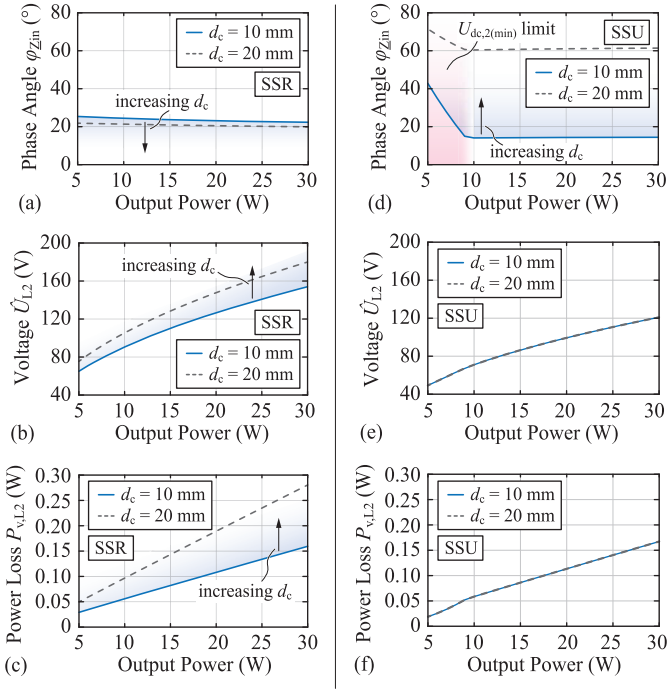

(g)

Type	Parameter	Value	Parameter	Value
SSR	C_1, C_2	2.20 nF	L_1, L_2	18.8, 18.4 µH
SSU	C_1, C_2	3.14 nF	f_0	800 kHz
	k_0	0.33	$k_{dc=10\,mm}$	0.489
	$U_{DC,2(min)}$	22.0 V	$k_{dc=20\,mm}$	0.263

Figure 7: Performance indicators for the SSR operation using the *efficiency optimal control* in (a)-(c), and the SSU operation using the *constant load impedance control* in (d)-(f), calculated for a variable output power and coil separation distances d_c of 10 mm and 20 mm, and the IPT resonant circuit parameters given in (g).

By introducing a lower limit for the secondary side DC-link voltage, the buck-boost converter on the primary and secondary side can be omitted and a simple bidirectional buck converter can be used for the battery charging converter and on the primary side, a simple boost converter can be employed. Hence, as shown in **Fig. 6**, the inverter and the buck-type battery charging converter are connected in parallel to the secondary side DC-link. The inductor used for the buck converter can then be designed for a lower power throughput and therefore allows for a smaller volume compared to the inductor of the secondary side buck-boost converter needed for the SSR IPT system shown in **Fig. 5**.

The control circuit of the battery charger continuously supervises the secondary side DC-link voltage $U_{DC,2}$ and if the voltage drops below the lower limit because the IPT system cannot transmit sufficient energy, the IPT system is disconnected from the DC-link using a load-switch and the battery charger takes over the power management and provides the energy supply for the LVAD inverter.

C. Discussion

Fig. 7(a)-(f) shows different performance indicators, which are particularly important for the TET system application at hand, calculated for the SSR and the SSU compensated IPT systems, using the previously explained control strategies. These indicators are the phase angle of the input impedance $\varphi_{\underline{Z},in}$, the secondary side coil peak voltage $\hat{U}_{L2}$ and the secondary side coil power loss $P_{v,L2}$, which are calculated for the IPT resonant circuit specifications shown in **Fig. 7(g)**, considering a variable output power and different coil separation distances d_c. The implications of the analysis are summarized in the following:

- **Phase angle of the input impedance:** The phase angle of the input impedance is directly related to the energy transfer efficiency. For the SSR compensation, using the *efficiency optimal control*, the phase angle of the input impedance is approximately constant, despite a varying output power, and is slightly decreasing with lower coil coupling factors (cf. **Fig. 7(a)**). In contrast, as shown in **Fig. 7(d)**, in case of the SSU compensation, the phase angle of the input impedance increases significantly at large coil separation distances, which in turn reduces the energy transfer efficiency.
- **Secondary side coil peak voltage:** A main disadvantage of the series-series compensated IPT system is the large IPT coil voltage amplitudes. Specifically on the secondary side, a large coil voltage bears several potential safety risks for the patient. The ISO 14708-1 international standard on the general requirements for safety of an active implantable medical device states, that any insulation of electrical conductors must withstand a dielectric strength test in which the applied voltage is no less than twice the peak voltage experienced by the part [26]. In order to maintain the mechanical flexibility of the implanted IPT coil, a silicone elastomer is preferably used for the encapsulation, which generally offers a very high dielectric strength of more than 20 kV/mm [27] and which is also available for medical device encapsulations [28]. Hence, an appropriate electrical insulation of the TET coils is easy to achieve. However, as shown in [29], the large secondary side coil voltage significantly contributes to the Electro-Magnetic Field (EMF) exposure of the human tissue, and hence, the secondary side coil voltage should be kept as low as possible. In case of the SSR compensated system, the secondary side coil peak voltage is increasing with increasing coil separation distance, as shown in **Fig. 7(b)**, which is due to the *efficiency optimal control*, where the equivalent load resistance is decreased with decreasing coil coupling factor. In contrast, the secondary side coil peak voltage of the SSU compensated system is independent of the coil separation distance, since the equivalent load resistance is kept constant, regardless of a varying coil coupling factor.
- **Secondary coil power loss:** Excessive heating of the human tissue surrounding the implanted IPT coil can cause discomfort to the patient or even permanent tissue damage. In case of the SSR IPT system, the secondary side coil power loss shows a proportionality according to $P_{v,L2} \propto P_2/k$. Consequently, the coil power loss is increasing substantially with increasing coil separation distance (cf. **Fig. 7(c)**), which is a main disadvantage of the SSR IPT system operation.

As with the secondary side coil peak voltage, the sec-

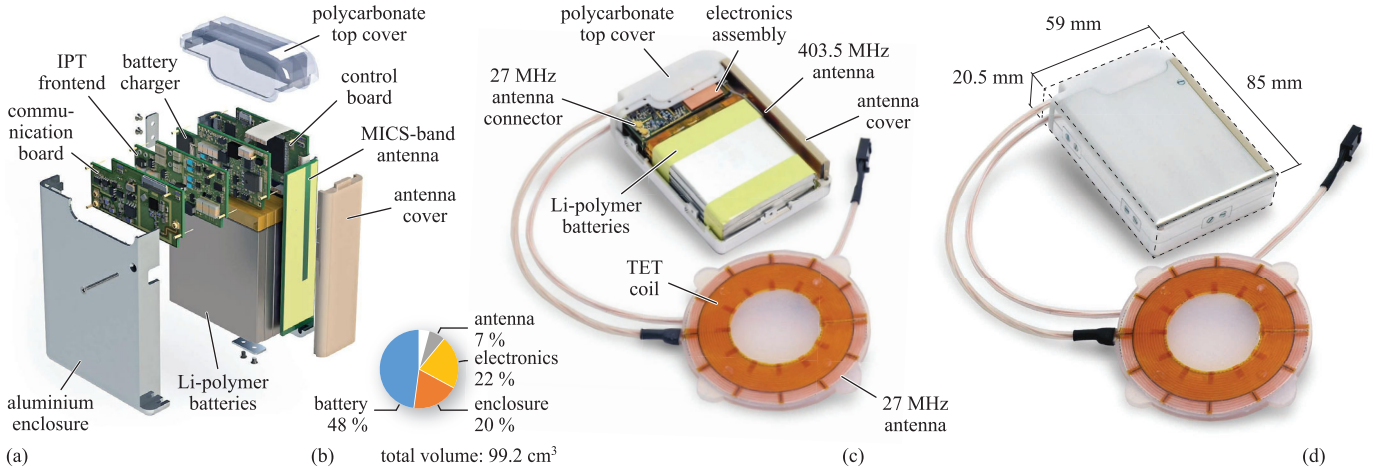

Figure 8: (a) Explosion view of the CAD drawing of the TET implant prototype. (b) Calculated TET implant volume distribution. (c)-(d) Hardware realization of the demonstrator prototype.

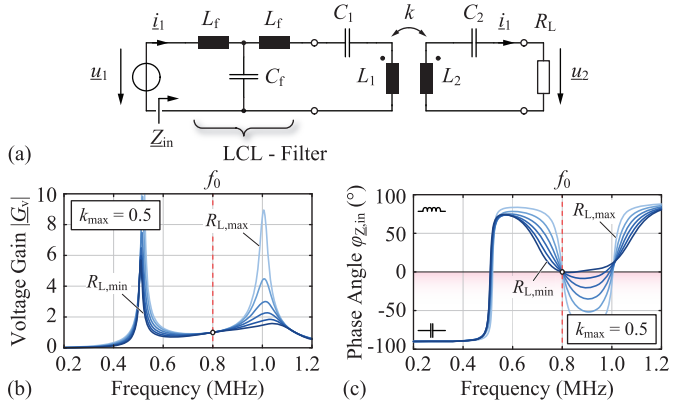

Figure 9: (a) Series compensated IPT system including an LCL-filter at the resonant circuit input, as it is proposed in [30]. (b)-(c) Corresponding voltage gain and phase angle of the input impedance for variable load conditions.

ondary side coil power loss of the SSU compensated IPT system is independent of the coil coupling factor and is only proportional to the output power. This clearly shows the main difference between the two systems. In case of the SSR compensation, the coil power losses are balanced between the primary and secondary side coil and are increasing simultaneously if the coil coupling factor decreases [18]. In contrast, in case of the SSU compensation, the power losses are asymmetrically distributed, i.e, with increasing coil separation distance, the primary side coil power losses are increasing significantly, but the secondary side coil power losses are not affected by a varying coil alignment.

In that sense, the power transfer capability of the SSR compensated system is mainly limited by the EMF exposure and the heating of the human tissue at increasing coil misalignment. In case of the SSU compensated system, the power transfer capability is limited by the primary side power losses and the maximum tolerable inverter input voltage.

In a recent publication in [30], it is proposed to include an LCL-filter circuit at the output of the primary side inverter (cf. **Fig. 9(a)**), which allows to convert the simple SSR compensated IPT circuit into a system with voltage source behaviour at the resonant frequency f_0 (cf. **Fig. 9(b)**). Furthermore, the circuit exhibits a purely resistive input impedance at the operating frequency despite of coil coupling- and output power variations (cf. **Fig. 9(c)**). However, the voltage gain is dependent on the IPT coil coupling and both the primary and secondary side DC-link voltages must be adapted in order to achieve an operation at the maximum energy transmission efficiency, as it is the case for the SSR IPT system.

In order to achieve a voltage gain of one at the resonant frequency, as it is shown in **Fig. 9(b)**, the filter inductors L_f must be chosen equal to the mutual inductance of the IPT coils. Considering the resonant circuit parameters in **Fig. 7(g)** given for the particular IPT system prototype at hand, the additional filter inductance values are 9.2 uH and are calculated for a maximum coupling factor of $k_{\max} = 0.5$.

The two high-frequency inductors L_f are in the main power path and hence significantly contribute to the primary side power losses of the IPT system which is a drawback of the LCL-filter solution. However, a final performance assessment of the concept requires an in-depth comparison, which is beyond the scope of this paper.

A particular challenge is the design of the TET system implant, because of the small available volume and the required high energy efficiency of the system, in order to prevent excessive heating of the surrounding tissue. Hence, it was decided to build a demonstrator prototype for the SSU TET system implant, because of the high secondary side power conversion efficiency and the reduced system complexity. The following section presents the design and the hardware realization of the TET implant. Subsequently, the overall TET system performance is experimentally verified.

III. Implant Demonstrator Prototype

The implant volume must be reduced as much as possible, in order to facilitate the implantation of the device and to increase the wearing comfort for the patient. Due to the large backup battery, the TET system implant is larger than

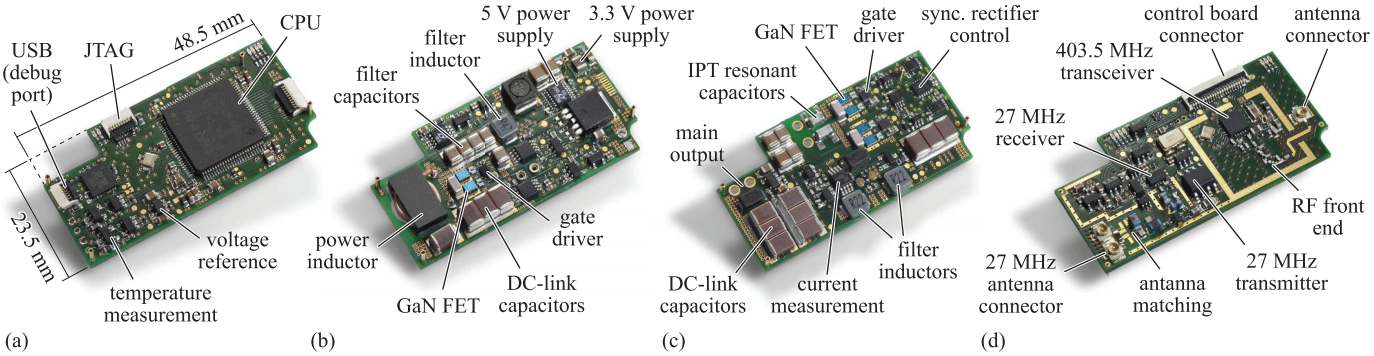

Figure 10: (a) Control board, (b) battery charging converter, (c) IPT energy receiver and (d) wireless communication electronics.

today's Implantable Cardioverter Defibrillators (ICDs), which can have a volume of less than 60 cm^3. In discussions with medical experts, it was concluded that a maximum volume of 100 cm^3 (10 cl) should be targeted for the TET implant. This volume should include all the electronic building blocks, such as the IPT energy receiver, the communication electronics and the backup battery as well as the control electronics. It is the opinion of the authors that the motor inverter should be integrated into the LVAD itself, since the inverter power losses could be removed more efficiently due to the continuous blood flow in the LVAD.

Fig. 8(a) shows the concept of the system integration. It was decided to use a modular design approach which allows for higher flexibility and a compact design. The functionality of the electronics is divided into four sub-modules. The four PCBs are stacked on top of each other and are interconnected using flat ribbon cables. The prototype implant enclosure is manufactured from aluminium and 3D-printed polycarbonate. As shown in **Fig. 8(b)**, the enclosure occupies almost the same volume as the electronics assembly. However, almost 50 % of the total implant volume is occupied by the backup battery. The final TET implant prototype with is depicted in **Fig. 8(c)** and **(d)**.

For the implant prototype it was decided to use a commercially available general purpose lithium-polymer battery. These batteries offer a high volumetric energy density and the battery cells can be manufactured in wide range of different shapes, which increase the design flexibility and reduce the prototyping cost. For the implant prototype, the lithium-polymer battery LP454854 is used, which has a nominal cell voltage of 3.7 V and a capacity of 1.7 Ah [31]. Four battery cells are connected in series, in order to achieve the nominal battery voltage of 14.8 V and in order to prevent battery damage, each battery includes an overcharge and -discharge protection circuit. The battery pack has a total boxed volume of about 4.8 cl, weighs 136 g and stores a nominal energy of 25.2 Wh.

The electronic sub-modules are shown in **Fig. 10**. For the implant control, an ARM Cortex-M4 CPU is used, which is placed on the control board shown in **Fig. 10(a)**. The microcontroller implements all the functionality needed to control the synchronous rectifier and the battery charging converter and provides the interface for the wireless communication.

Fig. 10(b) shows the bidirectional buck-type battery charging converter. In order to protect the battery from the large current ripple, an additional LC-filter stage is connected in series with the battery. The converter is operated at a switching frequency of 300 kHz and the EPC2016C GaN FETs are used for the switches. The inductor is built using an ER 11/5 ferrite core set and 13 turns of litz-wire consisting of 135 strands with a strand diameter of 40 µm. For the core, the TDK/EPCOS N87 ferrite material was selected. The measured inductance value is 27.9 µH and the inductor is designed such that the peak-to-peak inductor current ripple is about 70 % of the maximum average inductor current at a battery voltage of 14.8 V, a DC-link voltage of $U_{\mathrm{DC},2} = 40\,\mathrm{V}$ and a maximum output power of 25 W.

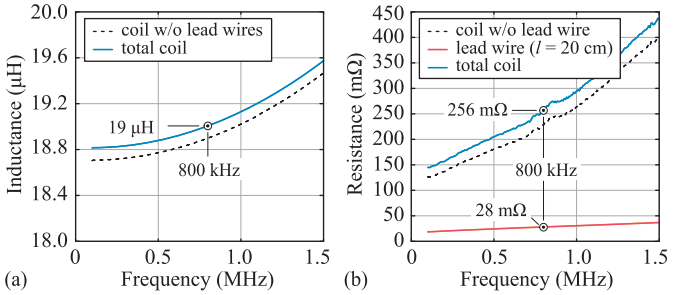

Figure 11: (a) Measured inductance and (b) AC resistance of the final implant TET coil prototype.

The main component of the IPT energy receiver PCB shown in **Fig. 10(c)** is the synchronous rectifier circuit presented in [25] and the secondary side compensation capacitors. In addition, current and voltage measurement circuits are included and a load switch allows to disconnect the IPT system from the load, whenever the LVAD is powered by the backup battery.

The circuits for the wireless communication are placed on the fourth PCB, depicted in **Fig. 10(d)**. The main Fadio Frequency (RF) transceiver is operated in the MICS-band at 403.5 MHz and is dedicated to the top-level communication. The implantable MICS-band antenna is integrated into the housing of the implant as shown in **Fig. 8(a)**. The design and characterization of the antenna are described in detail in [32]. In addition, a second bidirectional Near-Field Communication NFC channel is implemented. The loop-antennas are embedded directly into the TET coil prototypes. The NFC link operates in the ISM-band at 27 MHz and uses a simple On-Off-Keying (OOK) modulation scheme for the data

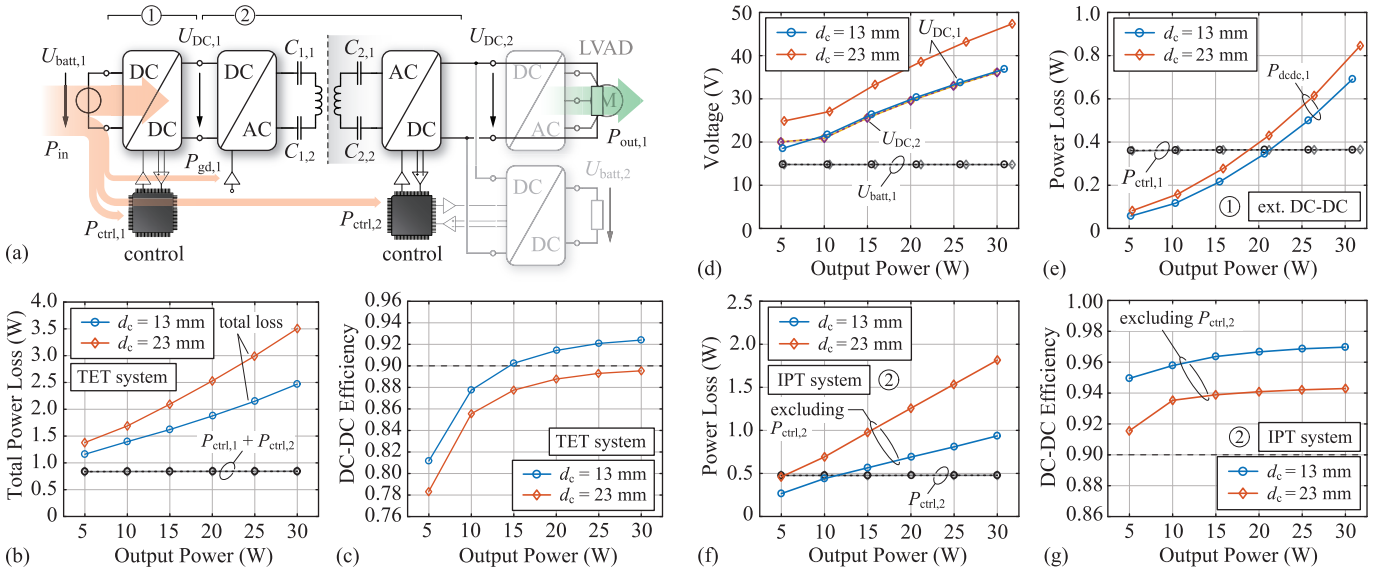

Figure 12: (a) Schematic circuit diagram of the SSU TET system prototype operated in *mode A*. (b) Measured total SSU TET system power loss and (c) total DC-DC efficiency. (d) Input and output voltage of the IPT system. (e) Power loss of the external boost-type DC-DC converter stage and the separately measured primary side control and auxiliary circuit power losses. (f) Power loss of the IPT system power stage, obtained from the measured inverter input power and rectifier output power, including the inverter gate drive power loss. The secondary side control and auxiliary circuit power losses are indicated in the same figure. (d) Corresponding DC-DC efficiency of the IPT system power stage, excluding the secondary side control losses.

transmission. However, the simple modulation scheme is prone to interferences with the switching noise of the IPT system and a careful NFC antenna design is required to electrically separate the NFC antennas from the TET coils as much as possible. The idea is to dedicate the NFC channel exclusively to the control of the IPT system, such that the MICS-band communication can be used for uncritical high-level tasks, such as the control of the LVAD and the monitoring of physiological sensor data.

The final implant TET coil prototype is shown in **Fig. 8(c)** and is identical to the external TET coil. The winding layer of both TET coils has an outside diameter of approximately 69 mm and an inside diameter of 35 mm. The single layered coils consist of 17 turns of litz-wire with 330 strands and a strand diameter of 40 µm. Finally, the coil windings are encapsulated in RTV-3428 A&B silicone [33]. Including the silicone encapsulation, the TET coils have an overall outside diameter of 73 mm, a thickness of 3 mm and a weight of 26 g. The measured inductance and AC resistance of the secondary side coil, with respect to the operating frequency, is shown in **Fig. 11(a)** and **(b)**, respectively. The lead wire length is 200 mm and its AC resistance was measured separately, using a twisted pair litz-wire cable of the same length. At the operating frequency of 800 kHz, the measured self-inductance and AC resistance of the primary side TET coil are 19.16 µH and 240 mΩ, respectively. In this case, the lead wires have a length of about 275 mm. The quality factors of the two coils are in a range of 373 to 401 at the operating frequency and the self-resonance frequency in air is about 6.85 MHz for both coils.

The dimensions of the final implant prototype are 85 mm×59 mm×20.5 mm (cf. **Fig. 8(d)**) and the boxed volume is 10.3 cl. The prototype implant has a weight of 188 g, which is mainly due to the large battery pack. It should be noted, that the implant prototype can be used for short-term in-vivo experiments when the backup battery is removed, but in its current state, the prototype is not hermetically sealed and is therefore not suited for long-term experiments.

IV. Performance Measurement

The following section provides a comprehensive experimental performance evaluation of the TET system prototype. First, the total TET system performance is determined for the SSU TET system and second, in order to have a comparison, the power loss an DC-DC efficiency is measured for the SSR TET system as well.

A. SSU TET System

For the proposed SSU TET system, two separate operating modes are considered. In the first mode, denoted with *mode A*, the power is delivered directly to the LVAD, without the operation of the backup battery charger. The second operating mode, denoted with *mode B*, considers a constant power supply for the LVAD and the simultaneous operation of the battery charger with variable output power.

The external part of the TET system is realized using the inverter circuit presented in [25]. The inverter stage is supplied by a boost converter, which is implemented with the same battery charger PCB as it is used for the TET implant prototype. The primary side DC-DC converter is operated in boost mode only and the boost inductance is optimized for a high power conversion efficiency, since in this case, the power density is of minor importance. The inductor is manufactured from two stacked EELP 14/3.5/5 core sets made of the N87

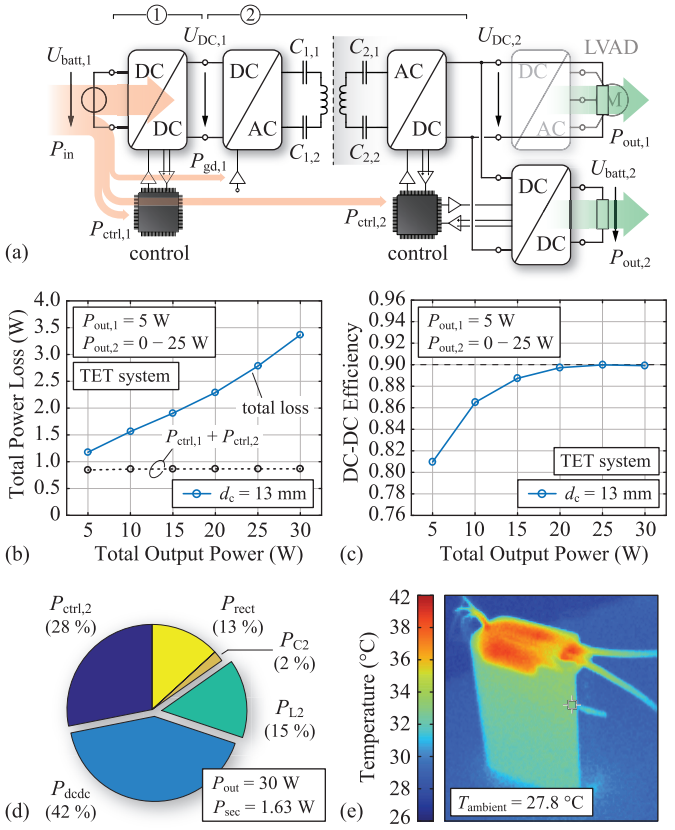

Figure 13: (a) Schematic circuit diagram of the SSU TET system prototype operated in *mode B*. (b) Total SSU TET system prototype power loss and (c) total DC-DC efficiency. (d) Calculated distribution of the implant power losses. (e) Thermal image of the implant hardware prototype, operated at a total output power of 30 W, including the battery charger output power of 25 W.

ferrite material. The winding is realized with 12 turns of litz-wire with 9 strands and 200 µm strand diameter. The air-gap of the inductor is adjusted such that the inductance value attains 39.7 µH at the operating frequency of 150 kHz.

The TET system performance was measured for a coil separation distance d_c of 13 mm and 23 mm, such that the distance between the TET coil encapsulations is exactly 10 mm and 20 mm. Accordingly, the measured coupling factors are 0.390 and 0.219, respectively. The primary and secondary side compensation capacitances $C_{1,1}$, $C_{1,2}$ and $C_{2,1}$, $C_{2,2}$ have a value of 5.6 nF each, and are designed for $k_0 = 0.262$. According to (22), the optimum secondary side DC-link voltage $U_{DC,2}$ at maximum output power is 36.2 V. The primary side inverter is operated at a switching frequency of 800 kHz and the dead-time of the switch control signals is set to 65 ns. The lower limit for the IPT system output voltage is set to $U_{DC,2} = 20$ V.

Fig. 12(a) illustrates the structure of the SSU TET system prototype for the operating *mode A*, where the power is transferred directly to the LVAD, without charging of the implant backup battery. The power loss components that are additionally considered for the total system input power P_{in} are the losses caused by the primary and secondary side control board, including auxiliary power supplies, measurement circuits, as well as the gate drivers for the boost converter and the IPT inverter stage, as indicated in **Fig. 12(a)**. Note that the power loss of 258 mW of the FPGA and its auxiliary power supplies, which generates the control signals for the full-bridge inverter, is not included in the performance evaluation, since in a final realization of the external control unit, the signals are generated directly by the MCU. Further, the wireless communication is not included in the performance measurements, and was disabled in the implant hardware prototype. The output power is measured at a load resistor, which models the power consumption of the LVAD. The external battery supply is replaced by a programmable laboratory DC power supply.

Fig. 12(b) shows the results of the total power loss measurement. The power loss was measured for an output power range of 5-30 W, but it is most unlikely that a single LVAD consumes more than 12 W. However, for systems providing biventricular support or for a TAH, the power consumption of the circulatory support system could reach up to 20 W or even more. The total measured power loss ranges from 1.16 W up to 3.51 W depending on the output power and coil separation distance. The total implant power loss at maximum output power is calculated as 0.917 W and is independent of the coil separation distance. It should be noted, that the constant power loss of the combined primary and secondary side control and auxiliary circuit losses reach about 840 mW and offer great potential for further optimization.

The resulting DC-DC efficiency is shown in **Fig. 12(c)**. At maximum output power, the efficiency reaches up to 92.4 %. However, due to the constant power losses, the efficiency drops down to 78.3-81.2 % at the minimum output power of 5 W and a coil separation distance of 23 mm and 13 mm, respectively.

The measured primary and secondary side DC-link voltages and the measured power loss of the primary side boost converter and the IPT system power stage are shown in **Fig. 12(d)-(g)**. The power losses are derived from the measurement of the input and output power of each of the individual power stage in **Fig. 12(a)**, denoted with 1 and 2. The control and auxiliary circuit power losses $P_{ctrl,1}$ and $P_{ctrl,2}$ are measured separately and are given in addition in **Fig. 12(e)** and **(f)**, respectively. As the only exception, the constant inverter gate drive power loss $P_{gd,1}$ of 75 mW is already included in the IPT stage power loss measurement.

As explained in **Section II-B**, the output voltage of the SSU TET system is varied according to the output power of the IPT system, and is limited to a minimum output voltage of 20 V. As already stated, a main disadvantage of the SSU TET system is the increasingly inductive behaviour of the input impedance of the IPT resonant circuit, when the coil separation distance is increased. Hence, at low coil coupling factors, the primary side DC-link voltage must be increased in order to maintain the required energy transfer across the skin. As a consequence, the power loss on the primary side increases significantly with increasing coil separation distance (cf. **Fig. 12(f)**). Nevertheless, the secondary side power losses are small and are independent of the coil separation distance.

As shown in **Fig. 12(g)**, the IPT power stage attains DC-DC efficiencies up to 97 % at the minimum coil separation distance of 13 mm. However, as explained above, the efficiency drops

significantly with decreasing coil coupling factor.

The SSU TET system performance was also measured for the *operating mode B*, which considers a constant power supply of 5 W for the LVAD and an additional variable battery charger output power. The TET system schematic and the considered input and output power components for the *operating mode B* are illustrated in **Fig. 13(a)**. For the measurements, both the LVAD and the backup battery are modeled with an adjustable load resistor. The battery charger is operated in buck mode and controls the output voltage to the nominal battery pack voltage of 14.8 V. The load resistance is varied such that the output power $P_{\mathrm{out},2}$ ranges from zero to 25 W. The power loss measurement was performed at a coil separation distance of 13 mm and the result is shown in **Fig. 13(b)**. The total primary and secondary side control and auxiliary circuit power losses attain a value of 866 mW and are indicated in the same figure. Again, the power losses of the wireless communication are not included in the measurement and the module is disabled in the implant prototype. Further it should be noted that due to the small phase angle of the input impedance of the IPT resonant circuit at the minimum coil separation distance, the primary side inverter is partially hard-switching at an IPT system output power of 10-30 W. However, the switch voltage at the hard-switching instant is in a range of 4.6-6.3 V and does not contribute significantly to the total power losses.

The total DC-DC efficiency in **Fig. 13(c)** confirms that the TET system prototype is able to deliver a constant power of 5 W to the LVAD and simultaneously, a power of up to 25 W can be delivered to the internal battery with a total DC-DC efficiency of up to 90 %.

The distribution of the secondary side power losses is shown in **Fig. 13(d)** and is calculated for the maximum output power using both measurements and numerical models. The estimated total secondary side power loss is about 1.63 W and the secondary side IPT coil power loss is calculated as 252 mW, which is only 15 % of the total secondary side losses. The power loss in the implant (excluding power losses in the implant battery) is 1.38 W and **Fig. 13(e)** shows the corresponding thermal image of the implant prototype operated at maximum output power. The maximum temperature at the top cover of the prototype reaches 42 °C in air and further efficiency improvements are required to reduce the temperature rise of the implant surface. However, a final assessment of the thermal safety of the TET implant prototype is beyond the scope of the paper and would require more complex thermal models of the human body, as well as additional information on the location of the implantation, i.e the type and structure of the surrounding tissue.

B. SSR TET System

In order to compare the performance of the SSU TET system prototype, the DC-DC efficiency was also measured for the SSR TET system operation. In this case, it was decided to use the existing hardware, such as the IPT prototype system shown in **Fig. 14(a)**, together with the IPT coils and the secondary side synchronous rectifier, presented in [25].

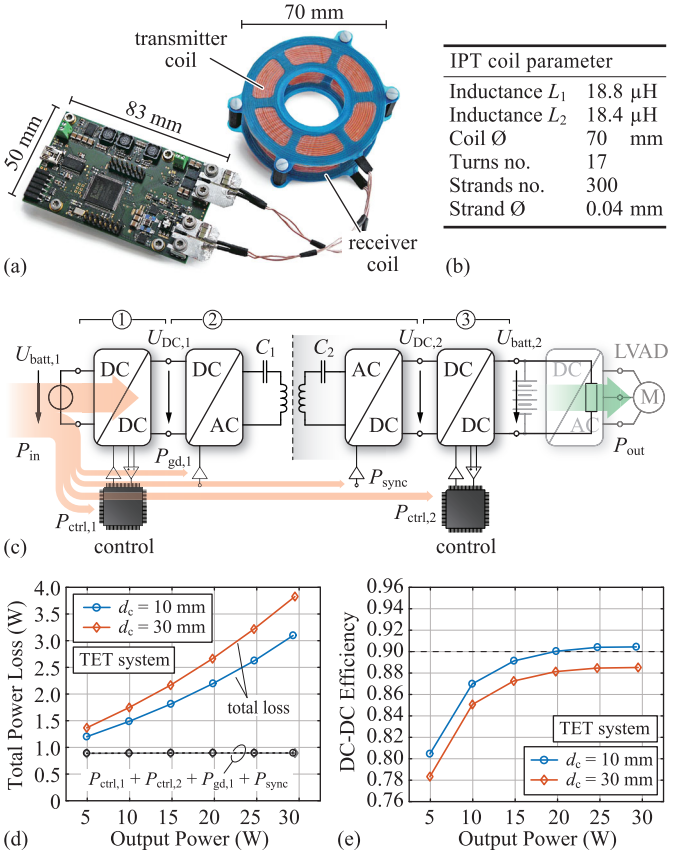

Figure 14: (a) Inverter and IPT coil prototypes presented in [25], which are used for the SSR TET system performance measurements. (b) Specifications of the IPT coil prototypes shown in (a). (c) Schematic circuit diagram of the SSR TET system prototype and the illustrated components of the input and output power considered for the total system performance evaluation. (d) Total SSR TET system prototype power loss and (e) corresponding total DC-DC efficiency.

The specifications of the IPT coil prototypes are given in **Fig. 14(b)**.

For the primary and secondary side DC-DC converter, the same battery charger PCB as for the TET implant prototype is used and is operated either in buck-, or with reversed terminal connections, in boost-mode, whichever is required for the operating point. The DC-DC converter stages are operated at 150 kHz and the same inductor is used as for the external DC-DC converter of the SSU TET system prototype. However, in this case, the power losses of the DC-DC converters are slightly underestimated, i.e. about 60 mW at maximum output power, because of the missing additional on-state resistance of the switch in continuous conduction mode, which is present in the conduction path of the idle branch of a four-switch buck-boost converter.

As described in [17], the IPT system is operated at 800 kHz and the total primary and secondary side compensation capacitances C_1 and C_2 have a value of 2.2 nF. A simplified schematic circuit diagram of the SSR TET system prototype is shown in **Fig. 14(c)**. The power loss measurements are performed for coil separation distances of 10 mm and 30 mm, which corresponds to coil coupling factors of 0.489 and 0.15 , respectively. The voltage at the load resistor is set to a constant value of 14.8 V, and the power at the load resistor is varied in

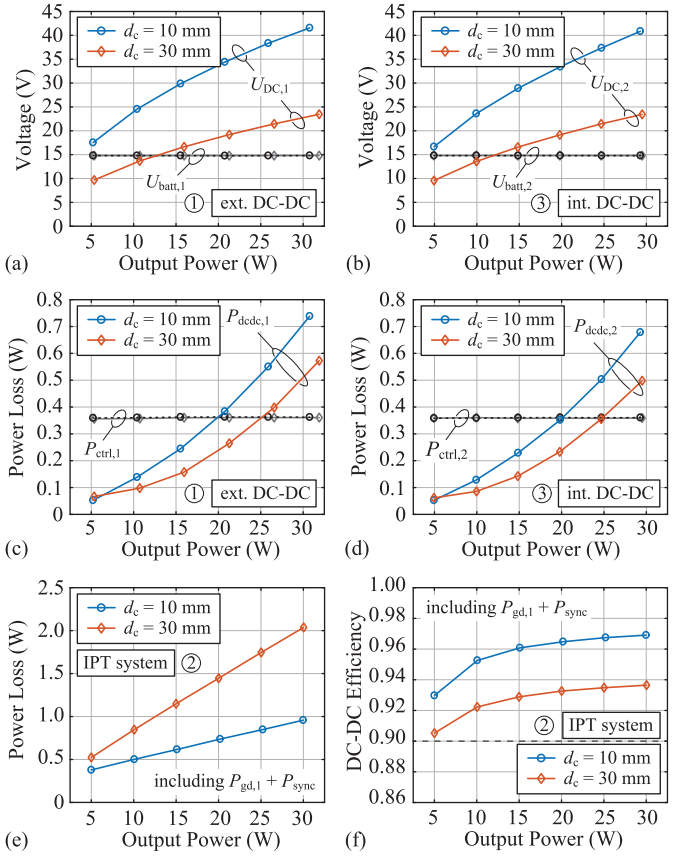

Figure 15: Performance measurement of the SSR TET system prototype. (a)-(b) Input and output voltage of the primary and secondary side DC-DC converter stages. (c) Power loss of the primary side and (d) of the secondary side DC-DC converter stage and the additional control and auxiliary circuit power losses. (e) Power loss of the SSR IPT system, including the inverter gate drive and the synchronous rectifier power losses. (f) Corresponding DC-DC efficiency.

a range of 5-30 W. In order to control the DC-DC converter stages, the same control board as for the SSU TET system prototype is used. The power loss is measured for each power conversion stage individually, which are denoted in **Fig. 14(c)** with numbers 1, 2 and 3.

The constant power losses P_{ctrl} of the control and the auxiliary circuits, which are used to operate the DC-DC converter stages, are measured separately. In addition, the primary side inverter gate drive power loss $P_{\mathrm{gd},1}$ and the secondary side synchronous rectifier gate drive and auxiliary circuit power losses P_{sync} are measured, and are included in the total IPT system power losses. Similar to the previous measurements, the power losses due to the wireless communication and due to the FPGA of the IPT inverter stage are not included in the performance evaluation.

The results for the total power loss measurement and the total system efficiency are shown in **Fig. 14(d)** and **(e)**, respectively. Due to the symmetry of the particular circuit, the power losses are distributed approximately in equal parts between the primary and secondary side. Therefore, it can be inferred with good approximation, that the implant power losses are about half of the measured total power losses. Again, as shown in **Fig. 14(d)**, the total constant power loss of 893 mW is rather high and allows for further improvement. The total DC-DC efficiency depicted in **Fig. 14(e)** reaches values of up to 90.4 % at maximum output power and minimum coil separation distance. And even at a large coil separation distance of 30 mm, efficiencies of up to 88.5 % are achieved.

Fig. 15(a) and **(b)** show the primary and secondary side input and output voltages $U_{\mathrm{batt},1}$ and $U_{\mathrm{batt},2}$, as well as the DC-link voltages $U_{\mathrm{DC},1}$ and $U_{\mathrm{DC},2}$ for the SSR TET system operation. As explained in **Section II**, at large coil separation distances, the primary and secondary side DC-link voltages are decreased in order to maintain an efficiency optimal operation. Accordingly, the overall IPT system efficiency is optimized, but the primary and secondary side coil power losses are increased simultaneously for a decreasing coil coupling factor and constant output power, which causes additional heating of the TET coils and hence, is a main disadvantage of the SSR TET system operation.

The primary and secondary side DC-DC converter power losses are shown in **Fig. 15(c)** and **(d)**, respectively. In addition, the total primary and secondary control and auxiliary circuit power losses are indicated in the same figures. The SSR TET system operation has the advantage, that at large coil separation distances, i.e. at low coil coupling factors, the DC-link voltage is decreased and hence reduces the switching losses in the DC-DC converter stages. The power loss of the IPT stage increases linearly with increasing output power, as shown in **Fig. 15(e)**. The active load matching which is a result of the *efficiency optimal control* of the SSR IPT system, allows to reduce the power losses significantly at large coil separation distances. As a result, the DC-DC efficiency of the IPT system, which is shown in **Fig. 15(f)**, is above 90 % even at a large coil separation distance of 30 mm, and reaches a maximum efficiency of up to 96.9 % at the minimum coil separation distance and maximum output power. At a coil separation distance of 50 mm, i.e. a coil coupling factor of only 6 %, and for an output power of 5 W, the DC-DC efficiency of the IPT stage is still 83.7 % and 85.2 % at 10 W output power. Consequently, the wireless power supply for the LVAD operation can be sustained even for significant coil misalignment. However, it should be noted that in this case, the primary side inverter is fully hard-switching, which is due to the small phase angle of the input impedance.

V. Conclusion

As shown in this paper, the SSR TET system offers an impressive performance regarding the energy transfer efficiency and regarding the coil misalignment tolerance. However, the main disadvantages of the SSR compensated system using the *efficiency optimal control* are

- the increased control effort, which requires an on-line estimation of the coil coupling factor.
- the increased size of the secondary side DC-DC converter.
- the increasing implant TET coil power loss and voltage stress at increasing coil separation distance and constant power transmission.

In contrast, the SSU TET system operation allows for a simplified control scheme, i.e. the *constant load impedance control*, without the need for a coil coupling estimation,

and offers a reduced hardware complexity. In addition, at constant power transmission, the SSU TET system offers a constant secondary side coil power loss, regardless of the coil separation distance. As a main disadvantage, the coil misalignment tolerance and the power transfer capability of the SSU compensated system is limited by the large reactive power on the primary side.

For the performance evaluation, a fully functional and compact TET implant prototype was realized, including the IPT synchronous rectifier circuit, the backup battery and its charging converter, the control circuit and two separate wireless communication interfaces, including the integrated antennas. In case of the SSU TET system prototype, at maximum output power, the overall DC-DC efficiency attains values of up to 89 % and 92.4 % for coil separation distances of 23 mm and 13 mm, respectively. In case of simultaneous battery charging converter operation, an overall DC-DC efficiency of up to 90 % was achieved at a maximum power transmission of 30 W and minimum coil separation distance of 13 mm.

At coil separation distances of 30 mm and 5 W output power, the SSR TET system achieves an overall DC-DC efficiency of 78.3 % (i.e. 1.37 W total power loss). At 10 mm coil separation distance, the system efficiency is as high as 90.4 % at the maximum power transmission of 30 W and drops to 88.5 % at 5 W output power. The DC-DC efficiency of the IPT power stage itself is very high and reaches values of up to 96.9 % at the minimum coil separation distance, and for coil separation distances smaller than 30 mm, the DC-DC efficiency is always above 90 %.

An improved coil misalignment tolerance is important to maintain the needed energy transfer capability, despite of the movements of the patient, and therefore, increases the usability of the TET system. The coil misalignment tolerance is therefore an important and decisive property, which allows to chose the most practical TET system design. As a final conclusion, it can be stated, that despite the numerous disadvantages, the SSR TET system outperforms the SSU system in terms of efficiency and coil misalignment, and hence, allows for an increased usability. In order to minimize the EMF exposure of the human tissue due to the increased implant coil peak voltage, an electrical shielding can be implemented as described in [29].

ACKNOWLEDGMENT

The authors gratefully acknowledge the financial support by the Baugarten Zurich foundation. This work is part of the Zurich Heart project under the umbrella of "University Medicine Zurich/Hochschulmedizin Zürich".

REFERENCES

[1] Eurotransplant, "Annual Report 2016," Eurotransplant International Foundation, Leiden, The Netherlands, Tech. Rep., 2017.

[2] B. H. Trachtenberg, A. Cordero-Reyes, B. Elias, and M. Loebe, "A review of infections in patients with left ventricular assist devices: Prevention, diagnosis and management," *Methodist DeBakey Cardiovascular Journal*, vol. 11, no. 1, pp. 28–32, 2015.

[3] D. J. Goldstein, D. Naftel, W. Holman, L. Bellumkonda, S. V. Pamboukian, F. D. Pagani, and J. Kirklin, "Continuous-flow devices and percutaneous site infections: Clinical outcomes," *J. Heart Lung Transpl.*, vol. 31, no. 11, pp. 1151 – 1157, 2012.

[4] J. C. Schuder, "Powering an artificial heart: Birth of the inductively coupled-radio frequency system in 1960," *Artif. Organs*, vol. 26, no. 11, pp. 909–915, 2002.

[5] T. Pirbodaghi, C. Cotter, and K. Bourque, "Power consumption of rotary blood pumps: Pulsatile versus constant-speed mode," *Artif. Organs*, vol. 38, no. 12, pp. 1024–1028, 2014.

[6] M. S. Slaughter and T. J. Myers, "Transcutaneous energy transmission for mechanical circulatory support systems: History, current status, and future prospects," *J. Card. Surg.*, vol. 25, no. 4, pp. 484–489, 2010.

[7] J. A. Miller, G. Bélanger, and T. Mussivand, "Development of an autotuned transcutaneous energy transfer system," *ASAIO J.*, vol. 39, no. 3, pp. 706–710, 1993.

[8] T. Mussivand *et al.*, "Transcutaneous energy transfer system performance evaluation," *Artif. Organs*, vol. 17, no. 11, pp. 940–947, 1993.

[9] C. C. Tsai, B. S. Chen, and C. M. Tsai, "Design of wireless transcutaneous energy transmission system for totally artificial hearts," in *Proc. of the IEEE Asia-Pacific Conf. on Circuits and Systems (APCCAS)*, 2000, pp. 646–649.

[10] H. Miura, S. Arai, Y. Kakubari, F. Sato, H. Matsuki, and T. Sato, "Improvement of the transcutaneous energy transmission system utilizing ferrite cored coils for artificial hearts," *IEEE Trans. Magn.*, vol. 42, no. 10, pp. 3578–3580, 2006.

[11] Q. Chen, S.-C. Wong, C. K. Tse, and X. Ruan, "Analysis, design, and control of a transcutaneous power regulator for artificial hearts," *IEEE Trans. Biomed. Circuits Syst.*, vol. 3, no. 1, pp. 23–31, 2009.

[12] E. Okamoto, Y. Yamamoto, Y. Akasaka, T. Motomura, Y. Mitamura, and Y. Nosé, "A new transcutaneous energy transmission system with hybrid energy coils for driving an implantable biventricular assist device," *Artif. Organs*, vol. 33, no. 8, pp. 622–626, 2009.

[13] T. D. Dissanayake, "An effective transcutaneous energy transfer (TET) system for artificial hearts," Ph.D. dissertation, Inst. Bioeng., Univ. Auckland, New Zealand, 2010.

[14] H. Y. Leung, D. M. Budgett, D. McCormick, and A. P. Hu, "Wireless power system for implantable heart pumps based on energy injection Control," in *Proc. of the Progress In Electromagnetics Research Symp. (PIERS)*, 2012, pp. 445–449.

[15] L. Lucke, J. Mondry, S. Scott, and W. Weiss, "A totally implantable controller for use with rotary LVADs," Minnetronix Inc., 2014. [Online]. Available: http://www.minnetronix.com/assets/documents/publications/totally-implantable-controller.pdf. [Accessed: Aug. 08, 2017].

[16] Y. Fu, L. Hu, X. Ruan, and X. Fu, "A transcutaneous energy transmission system for artificial heart adapting to changing impedance," *Artif. Organs*, vol. 39, no. 4, pp. 378–387, 2015.

[17] O. Knecht and J. W. Kolar, "Comparative evaluation of IPT resonant circuit topologies for wireless power supplies of implantable mechanical circulatory support systems," in *Proc. of the 32nd IEEE Applied Power Electronics Conf. and Expo. (APEC)*, 2017, pp. 3271–3278.

[18] R. Bosshard, "Multi-objective optimization of inductive power transfer systems for EV charging," Ph.D. dissertation, Dept. Elect. Eng., Swiss Federal Inst. Technol. Zurich (ETHZ), Switzerland, 2015.

[19] E. Waffenschmidt and T. Staring, "Limitation of inductive power transfer for consumer applications," in *Proc. of the 13th European Conf. on Power Electronics and Applications (EPE)*, 2009, pp. 1–10.

[20] R. Bosshard, T. Guillod, and J. W. Kolar, "Electromagnetic field patterns and energy flux of efficiency optimal inductive power transfer systems," *Electrical Engineering*, vol. 99, no. 3, p. 969–977, 2017.

[21] R. L. Steigerwald, "A comparison of half-bridge resonant converter topologies," *IEEE Trans. Power Electron.*, vol. 3, no. 2, pp. 174–182, 1988.

[22] I. Nam, R. Dougal, and E. Santi, "Optimal design method for series LCLC resonant converter based on analytical solutions for voltage gain resonant peaks," in *Proc. of the 28th IEEE Applied Power Electronics Conf. and Expo. (APEC)*, 2013, pp. 1429–1437.

[23] W. Zhang, S.-C. Wong, C. K. Tse, and Q. Chen, "Design for efficiency optimization and voltage controllability of series-series compensated inductive power transfer systems," *IEEE Trans. Power Electron.*, vol. 29, no. 1, pp. 191–200, 2014.

[24] ——, "Analysis and comparison of secondary series- and parallel-compensated inductive power transfer systems operating for optimal efficiency and load-independent voltage-transfer ratio," *IEEE Trans. Power Electron.*, vol. 29, no. 6, pp. 2979–2990, 2014.

[25] O. Knecht, R. Bosshard, and J. W. Kolar, "High-efficiency transcutaneous energy transfer for implantable mechanical heart support systems," *IEEE Trans. Power Electron.*, vol. 30, no. 11, pp. 6221–6236, 2015.

[26] International Organization for Standardization (ISO), "Implants for surgery - Active implantable medical devices - Part 1: General require-

ments for safety, marking and for information to be provided by the manufacturer". ISO 14708-1:2014, Geneva, Switzerland, Aug. 2014.
[27] Shin-Etsu Chemical Co., Ltd., "Characteristic properties of silicone rubber compounds," 2016. [Online]. Available: http://www.shinetsusilicone-global.com/catalog/pdf/rubber_e.pdf. [Accessed: Aug 16, 2017].
[28] Dow Corning Corporation, "Silastic MDX4-4210 biomedical grade elastomer data sheet," 2005. [Online]. Available: http://www.dowcorning.com/content/healthcare/healthrubber/rtv_elastomer.asp. [Accessed: Jun. 01, 2017].
[29] O. Knecht and J. W. Kolar, "Impact of transcutaneous energy transfer on the electric field and specific absorption rate in the human tissue," in *Proc. of the 41th Annu. Conf. of the IEEE Industrial Electronics Society (IECON)*, 2015, pp. 4977–4983.
[30] L. Jianyu, Y. Nan, and L. Kaiyu, "A novel resonant network for a WPT system with constant output voltage," in *Proc. of the IEEE Conf. on Energy Internet and Energy System Integration (EI2)*, 2017, pp. 1–5.
[31] LiPol Battery Company, Ltd., "Lithium Polymer Battery List 2015," 2015. [Online]. Available: http://www.lipolbattery.com/lipoly-battery.html. [Accessed: Nov. 4, 2016].
[32] O. Knecht, Y. Jundt, and J. W. Kolar, "Planar inverted-F antenna design for a fully implantable mechanical circulatory support system," in *Proc. of the 18th IEEE Int. Conf. on Industrial Technology (ICIT)*, 2017, pp. 1366–1371.
[33] Suter Kunststoffe AG, "Swiss-Composite SCS-RTV 3428 A&B technical datasheet," 2016. [Online]. Available: http://www.swiss-composite.ch/pdf/t-SCS-RTV-3428-e.pdf. [Accessed: Jun. 27, 2017].

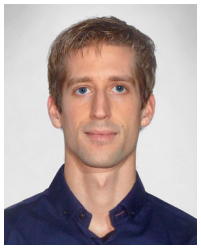

Oliver Knecht (S'14) received the M.Sc. degree in electrical engineering, in 2013, and the Ph.D. degree, in 2017, for the dissertation entitled 'Transcutaneous energy and information transfer for left ventricular assist devices' (accepted for publication), from the Swiss Federal Institute of Technology (ETH) Zurich, Switzerland. During his studies he focused on power electronics, control systems and microwave electronics. His research interests include the analysis, design and control of inductive power transfer systems for medical applications. In 2013, he joined the Power Electronic Systems Laboratory, ETH Zurich, where he was working towards the Ph.D degree, and in 2017, he joined Onefive GmbH (part of NKT Photonics A/S), where he is currently working as R&D engineer.

Johann W. Kolar (F'10) received his Ph.D. degree (*summa cum laude*) for the dissertation entitled 'VIENNA rectifier - Novel three-phase PWM rectifier systems with low effects on the mains' from the Vienna University of Technology, Austria. He is currently a Full Professor and the Head of the Power Electronic Systems Laboratory at the Swiss Federal Institute of Technology (ETH) Zurich. He has proposed numerous novel PWM converter topologies, and modulation and control concepts and has supervised over 70 Ph.D. students. He has published over 750 scientific papers in international journals and conference proceedings, 3 book chapters, and has filed more than 150 patents. He has presented over 20 educational seminars at leading international conferences, has served as IEEE PELS Distinguished Lecturer from 2012 through 2016, and has received 25 IEEE Transactions and Conference Prize Paper Awards, the 2014 IEEE Power Electronics Society R. David Middlebrook Achievement Award, the 2016 IEEE William E. Newell Power Electronics Award, the 2016 IEEE PEMC Council Award, and the ETH Zurich Golden Owl Award for excellence in teaching. He has initiated and/or is the founder of 4 ETH Spin-off companies. The focus of his current research is on ultra-compact and ultra-efficient SiC and GaN converter systems, wireless power transfer, Solid-State Transformers, Power Supplies on Chip, as well as ultra-high speed and ultra-light weight drives, bearingless motors, and energy harvesting.